UNIVERSITY OF LEEDS

This is a repository copy of *Resolving mercury cycling and the role of volcanism during the Toarcian Oceanic Anoxic Event*.

White Rose Research Online URL for this paper:
https://eprints.whiterose.ac.uk/224339/

Version: Accepted Version

Article:
Liu, J., Cao, J., Poulton, S.W. orcid.org/0000-0001-7621-189X et al. (5 more authors) (Accepted: 2025) Resolving mercury cycling and the role of volcanism during the Toarcian Oceanic Anoxic Event. Earth and Planetary Science Letters. ISSN 0012-821X (In Press)

This is an author produced version of an article accepted for publication in Earth and Planetary Science Letters, made available under the terms of the Creative Commons Attribution License (CC-BY), which permits unrestricted use, distribution and reproduction in any medium, provided the original work is properly cited.

Reuse
This article is distributed under the terms of the Creative Commons Attribution (CC BY) licence. This licence allows you to distribute, remix, tweak, and build upon the work, even commercially, as long as you credit the authors for the original work. More information and the full terms of the licence here: https://creativecommons.org/licenses/

Takedown
If you consider content in White Rose Research Online to be in breach of UK law, please notify us by emailing eprints@whiterose.ac.uk including the URL of the record and the reason for the withdrawal request.

White Rose university consortium
Universities of Leeds, Sheffield & York

eprints@whiterose.ac.uk
https://eprints.whiterose.ac.uk/

Resolving mercury cycling and the role of volcanism during the Toarcian Oceanic Anoxic Event

Jinchao Liu[a,b], Jian Cao[a,*], Simon W. Poulton[c, b], Wang Zheng[d], Jiubin Chen[d], Tianchen He[c], Guang Hu[e], Di Xiao[e]

[a] School of Earth Sciences and Engineering, Nanjing University, Nanjing 210023, China

[b] School of Earth and Environment, University of Leeds, Leeds, LS2 9JT, UK

[c] College of Oceanography, Hohai University, Nanjing 245700, China

[d] Institute of Surface-Earth System Science, Tianjin University, Tianjin 300072, China

[e] State Key Laboratory of Oil and Gas Reservoir Geology and Exploitation, Southwest Petroleum University, Chengdu 610500, China

ABSTRACT

The emplacement of the Ferrar large igneous province has been implicated as the ultimate driver of the Early Jurassic Toarcian Oceanic Anoxic Event. Mercury (Hg) systematics, alongside other lines of evidence, have been used to support this assumption, but controversy exists over the relative roles of volcanic versus terrestrial Hg inputs. Here, we investigate the Hg record in two cores that document a bathymetric transect across the lacustrine Sichuan Basin, China. Both cores are characterized by Hg accumulation during the Toarcian Oceanic Anoxic Event. However, observed negative correlations between Hg concentrations and geochemical indicators of water column sulfide availability suggest modification of primary Hg enrichments via redox-driven loss of Hg from the sediments. In addition, Hg isotope systematics show differing signals between the

shallow and deep cores, indicative of increased inputs from terrestrial and atmospheric sources, respectively. These results suggest that regional factors exert a major control on Hg enrichments in sediments, which must be considered when utilizing Hg systematics to evaluate volcanic activity. However, our approach highlights that lacustrine systems do document an important role for atmospheric Hg deposition during the Toarcian Oceanic Anoxic Event, confirming that large-scale activity of the Ferrar large igneous province was a key driver of this major environmental perturbation.

Keywords: Toarcian oceanic anoxic event; Mercury; Large igneous province; Redox conditions; Sichuan Basin

1. Introduction

During the early Toarcian Stage of the Jurassic (~183 million years ago, Ma), a major expansion of marine anoxia occurred during an interval known as the Toarcian Oceanic Anoxic Event (T-OAE; Jenkyns, 2010). The T-OAE coincided with intense global warming, an accelerated hydrological cycle, increased continental weathering, and increased marine productivity (Dera et al., 2009; Brazier et al., 2015; Xu et al., 2018; Bergman et al., 2021; Fernandez et al., 2021). The emplacement of the Ferrar large igneous province (LIP) in southern Gondwana at 182.779 ± 0.033 Ma to 182.430 ± 0.036 Ma, is commonly considered to have driven these extreme environmental perturbations (Moulin et al., 2011; Burgess et al., 2015; Kemp et al., 2024). Numerical simulations indicate that the Ferrar LIPs directly or indirectly led to the release of ~20,500 Gt of carbon (Heimdal et al., 2021), resulting in an increase in global atmospheric CO_2 of ~500 ppmv (Ruebsam et al., 2020).

Large-scale volcanism also often results in extensive release of gaseous monomeric mercury (Hg), and thus Hg enrichment in sediments has been widely used as a proxy for LIP activity (Pyle

and Mather, 2003; Grasby et al., 2013; 2019; Bagnato et al., 2014; Percival et al., 2015; 2018; Bergman et al., 2021; Edwards et al., 2021; Font et al., 2021; Shen et al., 2022). Indeed, Hg systematics have been used as evidence for enhanced volcanism as the driving mechanism for the T-OAE (Percival et al., 2015; Them et al., 2019; Font et al., 2022; Jin et al., 2022), along with several other major geological events (e.g., the Permian–Triassic Boundary Event, and the Triassic-Jurassic Boundary Event; Sanei et al., 2011; Grasby et al., 2017; 2019; Shen et al., 2019; 2022; Corso et al., 2020; Zhou et al., 2024). However, the application of Hg as an indicator for the role of enhanced volcanism during the T-OAE is controversial. Negative mass independent fractionation (MIF) of Hg isotopes (expressed as Δ^{199}Hg), found in the east tributary of Bighorn Creek, Canada and the Ordos Basin, China, have been taken as evidence that global enrichments in Hg during the Toarcian were related to terrestrial Hg inputs, which is supported by a lack of Hg enrichment in some proximal sections (Them et al., 2019; Jin et al., 2022). This phenomenon has also been observed during other major events, such as the Permo–Triassic Boundary Event, complicating the direct linkage between Hg records and LIPs (Grasby et al., 2017). This uncertainty as to whether LIP activity during geological events can be revealed by Hg enrichments, and to what extent regional factors (e.g., terrestrial input) may affect sedimentary Hg signals, severely limits our ability to evaluate controls on many major geological events.

Here, we report Hg systematics, including isotopic compositions, for two cores covering a shallow to deep lacustrine transect in the Toarcian Sichuan Basin, China. We investigate links between the Ferrar LIPs and the T-OAE, as well as regional controls on Hg cycling. Our approach addresses the distinct processes (i.e., terrestrial input versus atmospheric deposition) involved in Hg cycling, and hence resolves the role of volcanism as a driver of the T-OAE, with major implications for utilizing Hg systematics as a proxy for enhanced volcanism during other key intervals of global environmental change.

2. Geological setting and samples

The Sichuan Basin (Fig.1) transitioned to a terrestrial system during the Late Triassic due to uplift of the Yangtze Plate (Feng et al., 2015). During the Toarcian, freshwater lacustrine deposits of the Da'anzhai Member formed (Xu et al., 2017; Liu et al., 2020; Liu et al., 2022). At this time, the Sichuan Basin was a circular depression, with the sedimentary center located in the Yilong-Dazhou region (Deng et al., 1998; Li and He, 2014). Moving from the periphery towards the center of the basin, the depositional environments are represented by riverine conglomerates, shallow lake mudstone facies, shallow lake bioclastic limestone facies, and semi-deep to deep lake mudstone facies (Fig. 1B; Li and He, 2014). The Da'anzhai Member contains abundant bioclasts, including bivalve and ostracod shell fragments, as well as higher-plant debris and acritarchs (Fig. S1; Liu et al., 2020). Pyrite framboids are commonly observed (Fig. S1). In addition, highly elevated radiogenic initial $^{187}Os/^{188}Os$ compositions, an absence of biomarkers representing typical marine algae, and relatively stable pyrite sulfur isotopes and palaeo-salinity (e.g., B/Ga and Sr/Ba ratios) data (Xu et al., 2017; Liu et al., 2020; Qin et al., 2025), all suggest that, despite a global sea-level rise during the Early Jurassic, marine transgression had minimal impact on the Toarcian Sichuan Basin. Consequently, the Sichuan Basin is interpreted as a freshwater lake environment.

The two investigated sections include the X3 and LQ104X drill cores (Fig. 1). The X3 core is located close to Suining City, while the LQ104X core is situated close to Dazhou City, near the depositional center of the basin (Li and He, 2014; Fig. 1B). The two cores exhibit significant differences in lithological and sedimentary characteristics. Specifically, in the X3 core, the Da'anzhai Member was deposited in a shallow lacustrine facies and comprises a thick (ca. 30 m) fossiliferous limestone at its top, with shell-bearing mudstone or muddy fossiliferous limestone in its middle and bottom parts. In the LQ104X core, the Da'anzhai Member was deposited in deep or semi-deep lacustrine facies, comprising mudstone or shell-bearing mudstone, interbedded with very

thin shell layers (Fig. 2). Compared to the X3 core, the top of the LQ104X core does not exhibit the thick fossiliferous limestone but instead features relatively thin muddy fossiliferous limestone or shelly mudstone. Additionally, plant debris is more abundant in the X3 core than in the LQ104X core. Thus, based on the lithological and organic-petrological differences, the X3 core was deposited in a shallow lacustrine environment within the Sichuan Basin, whereas the LQ104X core represents deposition in a semi-deep to deep lacustrine environment (Fig. 1).

Based on Re–Os geochronology, the age of the Da'anzhai Member has been determined as 180 ± 3.2 Ma, indicating deposition during the late *tenuicostatum-falciferum* (*serpentinium*) zone of the Ammonite Province in northern Europe (Xu et al., 2017). In addition, the freshwater ostracod faunal assemblages (i.e., *Darwinula spp.* and *Metacypris unibulla*) and palynomorph assemblages (e.g., *Halosphaeropsis liassica*) indicates a late Early Jurassic age (Xu et al., 2017). This suggests that the deposition of the Da'anzhai Member in the Sichuan Basin was likely contemporaneous with the T-OAE. Hence, the basin appears to document a lacustrine record of the T-OAE (Xu et al., 2017; Liu et al., 2020; Liu et al., 2022).

3. Materials and methods

3.1. Materials

The studied samples (n = 121) were collected from the proximal X3 core and distal LQ104X core (Fig. 1B, C). Rock samples were crushed and ground to a particle size of less than 200 mesh using a silica mill, followed by oven drying at 60°C. Subsequently, all samples were analyzed for trace and major element contents, as well as Fe speciation. Additionally, 6 samples were analyzed for palynology, 79 samples were analyzed for Hg concentrations, and 21 samples were examined

for Hg isotopes. Total organic carbon and organic carbon isotope data for these samples are from published work (Liu et al., 2022).

3.2 Methods

3.2.1. Contents of $CaCO_3$

The contents of $CaCO_3$ were analyzed at Nanjing University. The powdered rock samples were treated with 2 M HCl at 60°C for 24 h to remove inorganic carbon, followed by rinsing with distilled water five times and drying for 72 h. The difference in mass before and after the hydrochloric acid treatment was then calculated to approximate the $CaCO_3$ contents of the samples.

3.2.2. Palynology

Palynological analysis was conducted at Nanjing Institute of Geology and Palaeontology, Chinese Academy of Sciences, China. Samples were processed using standard HF-HCl-HF palynological maceration techniques, which involved treating the samples with 30% HCl, followed by demineralization with 60% HF and repeated stirring. After washing with distilled water to neutral, organic matter was extracted from the residues via sieving (using 10 μm mesh), and concentrated via heavy liquid separation using a zinc bromide solution (D = 2.0). A Zeiss AX10 microscope was used for fossil identification.

3.2.3. Elemental analyses

Major and trace element contents were analyzed at the University of Leeds, UK. Bulk sediment digestions were performed on ~50 mg of ashed (550°C for 8 h) rock powder using HNO_3-HF-$HClO_4$ at ~70°C, followed by dissolution with H_3BO_3 and HCl. Total Al and Fe (Fe_T) contents

were measured by inductively coupled plasma optical emission spectrometry (ICP-OES), and Mo and U contents were measured by inductively coupled plasma mass spectrometry (ICP-MS). Rh was used as an internal standard to monitor signal drift during measurements. Total digests of a standard material (SBC-1) yielded values within the certified range for all elements (<5%), and replicate analyses gave a relative standard deviation (RSD) of < 3% for all elements of interest.

To constrain the degree of sediment enrichment relative to upper continental crust, enrichment factors (X_{EF}) were calculated as:

$$X_{EF} = \frac{\left(\frac{X}{Al}\right)_{sample}}{\left(\frac{X}{Al}\right)_{UCC}} \quad (1)$$

where *X* and *Al* represent the concentrations of elements X and Al, respectively (Tribovillard et al., 2013), and *UCC* is Upper Continental Crust (Rudnick and Gao, 2014). X_{EF} <1 and >1 imply that element *X* is depleted or enriched relative to UCC, respectively (Tribovillard et al., 2006).

3.2.4. Iron speciation analyses

We utilized a well-defined sequential extraction scheme to determine operationally-defined Fe pools, targeting carbonate associated iron (Fe_{carb}), ferric (oxyhydr)oxides (Fe_{ox}) and magnetite (Fe_{mag}) (Poulton and Canfield, 2005). Analyses were performed at the University of Leeds, with concentrations determined via atomic adsorption spectroscopy (AAS). Pyrite Fe (Fe_{py}) and pyrite S (S_{py}) contents were determined via a boiling chromous chloride distillation, after first checking for acid volatile sulfide phases (below detection in all samples) via a near-boiling 6 N HCl extraction (Canfield et al., 1986). International Fe speciation standard, WHIT (Alcott et al., 2020), was used to ensure accuracy, and replicate analyses gave a RSD of <5% for all Fe pools.

Extensive calibration in modern sediments and ancient marine rocks (Raiswell and Canfield, 1998; Poulton and Raiswell, 2002; Clarkson et al., 2014) has shown that highly reactive Fe (Fe_{HR}; calculated as $Fe_{carb} + Fe_{ox} + Fe_{mag} + Fe_{py}$) to Fe_T ratios >0.38 are commonly indicative of deposition from an anoxic water column, whereas ratios <0.22 are indicative of oxic deposition, while values between 0.22−0.38 are considered equivocal (Poulton and Canfield, 2011). For anoxic samples, ferruginous water column conditions are indicated by Fe_{py}/Fe_{HR} ratios <0.6, while euxinia is indicated by ratios >0.8, with values between 0.6-0.8 considered possibly euxinic (Poulton, 2021).

3.2.5. Defining regional oxic baseline values

Recent studies have highlighted that, wherever possible, redox parameters should be defined for the regional study area (Algeo and Li, 2020; Poulton, 2021; He et al., 2022; Li et al., 2024; Wang et al., 2024). In the case of the Sichuan Basin this is particularly important for U and Mo, since many of the samples, particularly those deposited before the T-OAE interval, have EF values <1. Since U and Mo are not mobilized and depleted from sediments under oxic conditions, these low EF values reflect low concentrations in the source material delivered to the basin, relative to UCC (Wang et al., 2024). We thus define oxic baseline thresholds for U_{EF} and Mo_{EF} by considering samples deposited before the T-OAE interval. These have low Fe_{HR}/Fe_T ratios (< 0.38) indicative of the oxic depositional conditions expected prior to the development of anoxia, giving oxic baseline values of 0.27 for U_{EF} and 0.56 for Mo_{EF}.

3.2.6. Mercury concentrations and isotopes

Mercury concentrations were analyzed at the State Key Laboratory of Pollution Control and Resource Reuse at Nanjing University, China. Approximately 50–100 mg of sample powder was

188 added to a measuring vessel and placed in a DMA-80 Direct Mercury Analyzer (Milestone Inc.;
189 Shelton, CT, USA) and step-heated. Volatilized Hg was collected by Au amalgamation prior to
190 spectral analysis. A total of 14 standards (LECO internal standard No. 502-685) were analyzed.
191 Specifically, five standards were analyzed prior to processing the samples and, throughout the
192 analyses, a duplicate sample and a standard were analyzed after approximately every tenth sample.
193 Values for all the standards were within specified limits (41±8 ng/g), with good reproducibility
194 between duplicate samples (see supplementary materials for details).

195 Mercury isotopes were analyzed at the School of Earth System Science at Tianjin University,
196 China. Before Hg isotope analysis, samples were first digested by reverse aqua regia, a mixture of
197 concentrated nitric acid (HNO_3) and hydrochloric acid (HCl) in a 2:1 ratio, and then the matrix was
198 removed using an ion exchange chromatographic method (Chen et al., 2010; Zheng et al., 2018).
199 Mercury isotopes were analyzed via multi-collector inductively coupled plasma mass spectrometry
200 (MC-ICP-MS, Neptune Plus, Thermo Scientific) following published methods (Shi et al., 2023).
201 Five Hg isotopes (^{198}Hg, ^{199}Hg, ^{200}Hg, ^{201}Hg and ^{202}Hg) and two Tl isotopes (^{203}Tl, ^{205}Tl) were
202 simultaneously measured.

203 Instrumental mass bias was corrected using a combination of internal correction with the
204 measured ^{205}Tl/^{203}Tl ratio (NIST SRM 997 Tl standard), and the standard-sample bracketing method
205 relative to the NIST 3133 Hg standard. The bracketing standard was matched to samples in terms of
206 both matrix and Hg concentration (less than 10% difference). On-peak blank corrections were
207 applied to all measured Hg isotopes. The Hg isotope compositions are expressed as delta (δ)
208 notations in units of per mil (‰) relative to the bracketing NIST 3133 Hg standard, as follows:

209 $$\delta^{x}Hg = \left[\frac{\left(\frac{^{x}Hg}{^{198}Hg}\right)_{sample}}{\left(\frac{^{x}Hg}{^{198}Hg}\right)_{standard}} - 1 \right] \times 1000 \quad (2)$$

where "^{x}Hg" represents ^{199}Hg, ^{200}Hg, ^{201}Hg or ^{202}Hg. The δ^{202}Hg composition is typically used to report mass-dependent fractionation (MDF). Any Hg isotope ratios that do not follow the MDF law were considered to be isotopic anomalies caused by mass-independent fractionation (MIF), which were calculated for ^{199}Hg, ^{200}Hg and ^{201}Hg, and expressed as per mil deviations from the predicted values based on the MDF law (Blum and Bergquist, 2007):

$$\Delta^{199}Hg = \delta^{199}Hg - 0.252 \times \delta^{202}Hg \quad (3)$$

$$\Delta^{200}Hg = \delta^{200}Hg - 0.502 \times \delta^{202}Hg \quad (4)$$

$$\Delta^{201}Hg = \delta^{201}Hg - 0.752 \times \delta^{202}Hg \quad (5)$$

To ensure precision and accuracy, the standard NIST SRM 8610 (UM-Almadèn standard) was measured after every 5 samples with mean values (2SD) of δ^{202}Hg = −0.53 ± 0.05‰, Δ^{199}Hg = −0.01 ± 0.06‰, and Δ^{200}Hg = 0 ± 0.04‰ (2SD, n = 48), consistent with published values (Bergquist and Blum, 2007).

3.2.8. Calculation of excess Hg (Hg_{ex})

Increasing $CaCO_3$ content can dilute the concentrations of organic or siliciclastic materials in sediments (Fendley et al., 2024). Given the presence of calcareous fossils, such as ostracods and bivalves, in the Da'anzhai Member, the assessment of element enrichment levels in the samples may be influenced by this dilution effect. This is supported by the negative correlations between $CaCO_3$ content and certain elements, including Scandium (Sc), Thorium (Th), Titanium (Ti), and Hg (Fig. S2). To account for this dilution, the contents of elements in the calcium carbonate-free portion of each sample (expressed as X_{cf}) were calculated using the following equation:

$$X_{cf} = \frac{X}{1 - \frac{CaCO_3}{100}} \quad (6)$$

where *X* represents the elements content in each sample.

For the calculation of Hg_{ex}, the background Hg contents (Hg_{bkg}) for each sample was first determined to represent the concentration prior to potential additions from volcanism or other sources. A best-fit curve between Hg_{cf} and the potential host phase (i.e., TOC_{cf}, $S_{py\text{-}cf}$ or Al_{cf}) for both the X3 core and LQ104X core was then established (Fig. S3). Following the suggestion that TOC_{cf} and Hg_{cf} follow either a hyperbolic tangent function or a logarithmic function (Fendley et al., 2024), both functions were applied by using the built-in Curve Fitting APP in MATLAB R2023b. The results indicate that the best-fit curve for TOC_{cf} and Hg_{cf} values in the Sichuan Basin follows hyperbolic tangent functions (Fig. S3). Using these best-fit functions, the Hg_{bkg} for each sample, was calculated as follows:

$$Hg_{bkg} = 98.70 \times \tanh\left(\frac{TOC_{cf}}{0.51}\right) - 45.86 \quad (7)$$

$$Hg_{bkg} = -112.08 \times \tanh\left(\frac{TOC_{cf}}{-0.96}\right) - 29.19 \quad (8)$$

where equations (7) and (8) apply specifically to the X3 core and the LQ104X core, respectively (Fig. S3).

Finally, subtracting Hg_{bkg} from the measured Hg content [Hg] of the sample yields Hg_{ex}:

$$Hg_{ex} = [Hg] - Hg_{bkg} \quad (9)$$

3.2.8. Binary isotopic mixing model

In this model, the contributions of the two Hg sources (i.e., atmospheric Hg deposition and terrestrial Hg input) to sediments can be estimated using a binary isotopic mixing model (Zheng et al., 2018):

$$f_{ter} \times \Delta_{ter}^{199} + f_{atm} \times \Delta_{atm}^{199} = \Delta_{sed}^{199} \quad (10)$$

where "f_{ter}" and "f_{atm}" are the fractions of terrestrial input and atmospheric deposition relative to total Hg, respectively, and $f_{ter} + f_{atm} = 1$. Δ_{ter}^{199} and Δ_{atm}^{199} are the Hg MIF signals of the two members. Δ_{sed}^{199} represents the $\Delta^{199}Hg$ values measured in the samples. In this study, simulations were performed on samples prior to the onset of Δ^{199}Hg depletion and on samples exhibiting the most negative Δ^{199}Hg values. According to Zheng et al. (2018), the selected values for the two end-members (i.e., terrestrial Hg and atmospheric Hg) are -0.26 ± 0.09‰ and 0.12 ± 0.05‰, respectively (Zheng et al., 2018). The model was executed using Monte-Carlo simulation.

4. Results and discussion

4.1. Geochemical evidences for the depositional setting of the two cores

The proximity of the two cores, X3 and LQ104X, to the palaeoshoreline is fundamental for subsequent discussions about Hg cycling in the Sichuan Basin during the T-OAE. In addition to lithological differences and the geographic setting (see above), geochemical signatures provide further evidence supporting their relative position in the basin. Firstly, the $CaCO_3$ contents differs significantly between the two cores, with the X3 core averaging 36.8 wt.% and LQ104X core averaging 25.4 wt.% (Fig. S4A). Given that shallow areas of the Sichuan Basin are characterised by a ring of bioclastic limestone facies, this likely indicates that the X3 core is closer to the palaeoshoreline.

Furthermore, Sc, Th and Ti are generally considered insoluble elements with low concentrations in the water column (Taylor and McLennan, 1985). These elements are frequently used as proxies for terrestrial input (Kamber and Webb, 2001; Kamber and Bolhar, 2004; Frimmel, 2009), and thus have the potential to determine the proximity of the two cores to the

279 palaeoshoreline. However, the high $CaCO_3$ content in some samples, particularly in the X3 core,
280 results in dilution of these elements in the Da'anzhai Member (Fig. S2), which may complicate the
281 determination of terrestrial inputs. To account for this dilution effect, Sc_{cf}, Th_{cf} and Ti_{cf} were
282 calculated (see Methods). The results show that Sc_{cf}, Th_{cf} and Ti_{cf} values in the X3 core are
283 consistently higher than those in the LQ104X core (Fig. S4B-D). Specifically, the average values of
284 Sc_{cf}, Th_{cf}, and Ti_{cf} in the X3 core are 30.7 ppm, 17.7 ppm, and 0.41 wt.%, respectively, while the
285 averages in the LQ104X core are 21.3 ppm, 15.3 ppm, and 0.38 wt.%, respectively. These findings
286 suggest that the X3 core received a greater proportion of terrestrial material compared to the
287 LQ104X core.
288 Thus, in combination with the geological setting, lithological differences and geochemical
289 data, it can be concluded that the X3 core is situated in a more proximal setting, closer to the
290 palaeoshoreline, whereas the LQ104X core is located in a more distal position.
291
292 *4.2. Expression of the T-OAE in the Sichuan Basin*
293 The T-OAE is characterized by a negative carbon isotope excursion (NCIE) and enhanced
294 organic matter accumulation in strata worldwide, due to a massive injection of isotopically light
295 carbon (^{12}C) into the atmosphere-marine system (Hesselbo et al., 2000; McElwain et al., 2005;
296 Jenkyns, 2010). The X3 core and LQ104X core from the Sichuan Basin exhibit significant negative
297 organic carbon isotope excursions at depths of 1785.90–1818.85 m and 3516.10–3546.95 m,
298 respectively (Liu et al., 2020; 2022; Fig. 2). Specifically, the negative carbon isotope excursion in
299 the X3 core has a magnitude of 3.85‰ and a thickness of 32.95 m, while the LQ104X core shows a
300 negative excursion of 3.74‰ with a thickness of 30.85 m (Liu et al., 2020; 2022). These values are
301 closely aligned, and both are accompanied by organic matter accumulation. In the X3 core, the TOC

contents increase from 0.34 wt% to 2.45 wt%, and in the LQ104X core, TOC rises from 0.09 wt% to 2.69 wt% (Liu et al., 2020; 2022). These similar isotope excursions and TOC enrichments suggest that the X3 and LQ104X cores are likely temporally consistent. In addition, these features are consistent with the typical T-OAE profiles observed in the western Tethys (i.e., Yorkshire, UK, and Dotternhausen, Germany). More importantly, the sedimentation rate in the Da'anzhai Member in the Sichuan Basin, estimated at 149.62 m/Ma based on cyclostratigraphy (Li, 2016), suggests that the duration of the negative organic carbon isotope excursions in the two Sichuan Basin wells was approximately 220 kyr, which is close to the T-OAE duration (288 ± 119 kyr; Kemp et al., 2024).

Additionally, the palynomorph assemblages from the X3 and LQ104X cores exhibit similarities to those from cores A and B in the study of Xu et al. (2017), reinforcing the interpretation of a Toarcian age (Fig. S5). Specifically, the dominant taxon is *Classopollis spp.* (89.2 %), followed by other gymnosperm pollen types, such as *Cerebropollenites carlylensis* and *Chasmatosporites elegans*, as well as pteridophyte spores such as *Cyathidites and Cibotiumspora juncta* (Fig. S5). A minor presence of *Veryhachium spp.* is also observed (Fig. S5). Significantly, the absence of the characteristic Araucarian pollen genus *Callialasporites*, a well-established marker for the Middle Jurassic (Srivastava, 1987; 2011; Riding and Shaw, 1991), further supports the assignment of the Da'anzhai Member to the Toarcian. Consequently, it is highly plausible that the Da'anzhai Member of the X3 and LQ104X cores records the T-OAE. However, it is crucial to emphasize that the stratigraphic framework of the Da'anzhai Member requires further refinement, particularly with regard to more accurate isotopic dating.

In summary, based on organic carbon isotopes, TOC contents, and palynological observations for the Da'anzhai Member, the T-OAE is likely recorded in the 1785.90–1818.85 m interval of the X3 core and the 3516.10–3546.95 m interval of the LQ104X core (Fig. 2; Liu et al., 2020; 2022).

During the T-OAE, redox changes were widespread in the marine realm, with transitions from oxic to anoxic-ferruginous (Fe-containing) or euxinic (sulphidic) water column conditions (Fernández-Martínez et al., 2023). To evaluate potential redox changes in the lacustrine Sichuan Basin, we follow recent suggestions and practice (Algeo and Li, 2020; Poulton, 2021; He et al., 2022; Li et al., 2024; Wang et al., 2024), by combining redox sensitive trace metal (U and Mo, expressed as enrichment factors; EFs) and Fe speciation systematics to provide the most robust redox reconstruction, which we interpret based on regionally-defined oxic baselines for these parameters (Fig. 2; see supplementary materials for details).

For the shallower X3 core, ratios of highly reactive iron over total iron (Fe_{HR}/Fe_T) show considerable scatter, with values commonly falling either in the equivocal (0.22–0.38) or anoxic (>0.38) zones (Fig. 2). However, when considered alongside U_{EF} values, consistent redox behaviour is observed. Low Fe_{HR}/Fe_T ratios and low U_{EF} values at the base of the section and immediately prior to the T-OAE suggest dominantly oxic deposition (Fig. 2). However, elevated values in the interim suggest an interval of water column anoxia, with low Fe_{py}/Fe_{HR} ratios and low Mo_{EF} values indicating ferruginous conditions. During the earlier stages of the T-OAE, oxic conditions are indicated by low Fe_{HR}/Fe_T ratios and low U_{EF} values. However, a transition to conditions that fluctuated between oxic and anoxic is indicated in the upper part of the T-OAE interval. Here, variable Fe_{py}/Fe_{HR} ratios and Mo_{EF} values indicate that when anoxic, the water column fluctuated between ferruginous and euxinic depositional conditions (Fig. 2). Above the T-OAE interval, fluctuations between ferruginous anoxia and oxic conditions are indicated by variable Fe_{HR}/Fe_T ratios and U_{EF} values, and mostly low Fe_{py}/Fe_{HR} ratios and Mo_{EF} values.

Similar trends are observed in the deep LQ104X core, but with notable differences. Specifically, while the pre-T-OAE oxic interval is also documented in the deeper water section, and

348 the T-OAE itself is characterized by alternating redox conditions, anoxia is more prevalent in the
349 earlier part of the T-OAE, which again fluctuated between euxinic and (mainly) ferruginous (Fig.
350 2). Redox conditions above the T-OAE interval are more difficult to resolve, since low Fe_{HR}/Fe_T
351 ratios contrast with relatively high U_{EF} values. However, these contrasting signals may potentially
352 be explained by a general decrease in the intensity of reducing conditions (i.e., no evidence for
353 euxinia) after the T-OAE, where anoxic conditions in deeper waters (indicated by elevated U_{EF}
354 values) promoted Fe_{HR} mobilization (as dissolved Fe^{2+}) from the sediments to the water column
355 (giving low Fe_{HR}/Fe_T ratios; Poulton, 2021). This Fe^{2+} then appears to have upwelled and
356 precipitated in shallower waters, resulting in the Fe_{HR} enrichments observed in core X3 (Fig. 2).
357 The temporal variability in the onset of anoxia in shallower and deeper settings during the T-
358 OAE interval may reflect the enhanced disconnect between deeper water settings and the
359 atmosphere, suggesting that anoxia was initiated in deeper settings. In addition, however, proposed
360 lake-level fluctuations in the Sichuan Basin across the T-OAE (Liu et al., 2020) likely also
361 contributed. During the initial stages of the T-OAE, the lake level was relatively shallow, with the
362 X3 core apparently situated above the chemocline, with anoxic ferruginous deeper waters. As the T-
363 OAE progressed and the lake level continued to rise (Liu et al., 2020), the shallower site also
364 became bathed in anoxic waters.
365
366 *4.3. Hg host phases and chemostratigraphy*
367 Before interpreting chemostratigraphic trends in Hg data (Fig. 2), it is important to consider the
368 host phase(s) of the Hg, in order to avoid potential misinterpretation of Hg anomalies (Grasby et al.,
369 2019; Shen et al., 2020b; Chen et al., 2023). Organic matter is generally recognized as the dominant
370 host of Hg in sediments, and thus data are normally presented on a total organic carbon (TOC)

normalized basis (Percival et al., 2015; Them et al., 2019; Font et al., 2022). In addition, however, Hg can also be hosted by sulfides and clay minerals (Outridge et al., 2007; Sanei et al., 2011). We thus explore the potential host phases in Fig. 3, which shows that when considering the entire data-set in the shallow X3 core (black lines), the strongest correlation exists between Hg concentrations and TOC ($R^2 = 0.66$; Fig. 3A), with weaker (but positive) correlations between Hg concentrations and both pyrite sulfur (S_{py}; $R^2 = 0.32$; Fig.3B) and aluminum (Al; $R^2 = 0.54$; Fig. 3C), likely indicating complexity in the host phase. In the deep LQ104X core, correlations are stronger between Hg concentrations and S_{py} ($R^2 = 0.59$; Fig. 3E), weaker for TOC ($R^2 = 0.45$; Fig. 3E), and particularly weak for Al ($R^2 = 0.16$; Fig. 3F), suggesting that Hg is dominantly associated with sulfides, with some Hg also present in association with organic matter.

In addition, there is distinct variability in Hg host phases through the stratigraphic profile, particularly in the deep LQ104X core. In this core (but note that similar trends are also observed in the X3 core), significant correlations between Hg concentrations and TOC ($R^2 = 0.77$) are evident during the non-T-OAE intervals (Fig. 3D). However, during the T-OAE, Hg concentrations show only a weak correlation with TOC contents ($R^2 = 0.24$; Fig. 3D), and instead there is a stronger correlation with S_{py} contents ($R^2 = 0.49$; Fig. 3E), suggesting a shift in the main Hg host phase. Generally, Hg exhibits the highest affinity for organic matter, but the affinity between Hg and sulfide minerals increases under euxinic conditions (Ravichandran, 2004). Thus, the increase in the proportion of Hg associated with pyrite sulfur during the T-OAE interval is entirely consistent with the observed redox transition and ensuing enhanced sulfide availability (Shen et al., 2020a) (Fig. 2). Overall, Hg appears to be dominantly hosted by organic matter in shallow areas, and by sulfide phases in deeper areas, at least in this lake.

393 Considering that the Hg host phases in the Sichuan Basin across the T-OAE are complex, it is
394 challenging to describe the extent of Hg enrichment using conventional ratios such as Hg/TOC,
395 Hg/TS or Hg/Al. In addition, the host phase-overprint (e.g., TOC-overprint and TS-overprint)
396 caused by the synergistic increases in Hg and host-phase proxies (e.g., TOC and TS contents) can
397 result in an underestimation of the degree of Hg enrichment (Percival et al., 2015; Charbonnier and
398 Föllmi, 2017; Frieling et al., 2023). Notably, this situation was prevalent during the T-OAE.
399 Specifically, while the massive activity of the Ferrar LIP would be expected to result in worldwide
400 Hg enrichments, not all T-OAE profiles exhibit elevated Hg/TOC ratios, including in the Yorkshire
401 (UK), Sancerre (France) and Dotternhausen (Germany) sections of western Tethys (see
402 Supplementary Information for details; Fig. 1A; Percival et al., 2015; Them et al., 2019). This may
403 be attributed to the exceptionally high TOC content (over 15 wt.%) that developed in a black shale
404 belt formed in the western Tethys during the T-OAE (Hermoso et al., 2009). Therefore, although Hg
405 concentrations in all three profiles show a notable increase, Hg/TOC values remain constant and
406 low due to the simultaneous substantial increase in TOC burial (Fig. 4; Percival et al., 2015; Them
407 et al., 2019).
408 Given this consideration, we instead utilize excess Hg (Hg_{ex}) values, calculated relative to
409 TOC contents, to quantify the extent of Hg enrichment(Fendley et al., 2024) (see Methods for the
410 calculation). This approach shows no significant correlation between Hg_{ex} and other host phase
411 proxies (i.e., S_{py} and Al contents) in the Sichuan Basin (Fig. S6), similar to the Cardigan Bay Basin,
412 Wales (Fendley et al., 2024). Consequently, Hg_{ex} can be effectively utilized to trace Hg enrichments
413 despite interferences arising from changes in the Hg host phase.
414 During the T-OAE, both the X3 core and LQ104X core exhibit elevated Hg_{ex}, combined with
415 increased Hg concentrations and Hg/TOC ratios (Fig. 2). Notably, three significant spikes are

observed in both cores (at 1816.25 m, 1806.50–1803.30 m and 1797.15–1796.10 m in the shallow X3 core, and 3542.46 m, 3530.95 m and 3522.05 m in the deep LQ104X core; Fig. 2). Based on our redox proxy data, the redox conditions of the Hg-enriched samples in the Sichuan Basin are characterized as ferruginous or weakly euxinic, which may promote mercury burial by enhancing the accumulation of organic matter and sulfides (Sanei et al., 2011). However, it is noteworthy that these Hg-enriched samples do not show a significant positive correlation with redox condition indicators (Fig. S7), suggesting that the shifts in redox conditions during the T-OAE were not the primary mechanism for Hg enrichment in the Sichuan Basin. Nevertheless, the transition in redox conditions, particularly the development of euxinia, would inevitably lead to an increase in mercury bound as sulfides in the sediments (Shen et al., 2020a; Fig. 3).

Additionally, calculated Hg_{ex} values for the Yorkshire, Sancerre and Dotternhausen profiles are consistent with the Sichuan Basin results, showing multiple Hg_{ex} spikes, including at -0.74–2.4 m in Yorkshire, 348.0–346.2 m in Sancerre, and 335–405 m in Dotternhausen (Fig. 4). This confirms extensive Hg enrichment at these sites during the T-OAE, which is masked when the data are normalized to TOC.

4.4. Pathways of Hg delivery to the Sichuan Basin

The main source of Hg to the atmosphere is from volcanism in pre-anthropogenic timescales, and thus the massive activity of the Ferrar LIP, would be expected to provide a major source of Hg (Blum et al., 2014; Yin et al., 2016). Subsequently, Hg emitted from volcanoes (be it LIPs or otherwise) enters oceans or lakes through terrestrial inputs and atmospheric deposition (Blum et al., 2014). Therefore, determining the pathways of Hg delivery is crucial for exploring potential links between Hg accumulation and volcanism.

439 The most effective method for distinguishing terrestrial input from atmospheric deposition is to
440 employ mass-independent fractionation (MIF) of odd-numbered Hg isotopes (expressed as Δ^{199}Hg;
441 Blum et al., 2014). The photochemical reduction ($Hg^{2+} \rightarrow Hg_{(g)}^{0}$) of Hg in the atmosphere can lead
442 to negative and positive Δ^{199}Hg values in gaseous Hg^0 and reactive Hg (including Hg^{2+} and
443 particulate Hg), respectively. The former is easily absorbed by plants, entering oceans or lakes
444 through terrestrial input, while the latter enters oceans or lakes through wet or dry atmospheric
445 deposition (Blum and Bergquist, 2007; Zheng and Hintelmann, 2009; Blum et al., 2014; Zheng et
446 al., 2018).
447 In the Sichuan Basin, the shallow X3 core exhibits an average Δ^{199}Hg value of 0.105‰, while
448 the deep LQ104X core has an average of 0.014 ‰. A two-way t-test indicates a statistically
449 significant difference in Hg isotopes between the two cores at the 99% confidence level (see
450 supplementary materials for details), suggesting that the Hg sources in these cores likely differ.
451 Furthermore, Δ^{199}Hg compositions in the shallow X3 core align with the east tributary of Bighorn
452 Creek, Canada, and the Anya section, China (Them et al., 2019; Jin et al., 2022), showing negative
453 excursions shifting from 0.13‰ to 0.04‰ (Fig. 2), and suggesting increased terrestrial Hg input
454 into the shallow area (Them et al., 2019). By contrast, the deep LQ104X core displays more
455 prominent Hg enrichment and significant positive Δ^{199}Hg excursions, shifting from 0‰ to 0.07‰,
456 indicating an increase in atmospheric Hg deposition (Fig. 2). These findings are further
457 substantiated by even-numbered MIF signals (expressed as Δ^{200}Hg), which exhibit trends similar to
458 Δ^{199}Hg (Chen et al., 2012; Zerkle et al., 2020) (Fig. 2). Specifically, during the T-OAE, Δ^{200}Hg
459 values in the shallow X3 core exhibit negative excursions, shifting from 0.05‰ to -0.01‰, while
460 Δ^{200}Hg values in the LQ104X core show positive excursions, shifting from -0.01‰ to 0.06‰.
461 These observations are further supported by relationships between Hg and Al. Mercury

462 concentrations for the non-T-OAE samples in the two cores exhibit a strong correlation with Al
463 contents, but the T-OAE samples show diverse behaviour between the two cores (Fig. 3E, F).
464 Specifically, Hg concentrations in the shallow T-OAE samples remain correlated with Al (R^2 =
465 0.53), while the deep samples show little correlation with Al (R^2 = 0.18; Fig. 3E, F), suggesting a
466 decoupling of Hg from clay minerals and a weak terrestrial influx in the deep area during the T-
467 OAE. Thus, Hg enrichment in the deep area was primarily controlled by enhanced atmospheric Hg
468 deposition, while in shallow areas it was related to an increased terrestrial influx.
469 Furthermore, we quantitatively simulated variability in terrestrial and atmospheric
470 contributions to Hg accumulation during the T-OAE in the two cores by applying a binary isotopic
471 mixing model, executed via Monte-Carlo simulation (see Methods; Zheng et al., 2018). This model
472 considers atmospheric deposition and terrestrial input as two end-members. The mixing model
473 suggests that, in the X3 core, the terrestrial input contribution (f_{ter}) increased from 13.9 ± 8.2%
474 (1SD) to 21.7 ± 10.2% (1SD) during the T-OAE (Fig. S8), while in the LQ104X core, atmospheric
475 deposition (f_{atm}) increased from 70.7 ± 11.0% (1SD) to 84.4 ± 8.7% (1SD) during the T-OAE (Fig.
476 S9). Notably, although terrestrial Hg input increased in the shallow X3 core during the T-OAE,
477 atmospheric Hg deposition remained the dominant source, as indicated by an f_{ter} value of < 50%.
478 This indicates that the Hg enrichments in the Sichuan Basin during the T-OAE was primarily related
479 to atmospheric Hg deposition. This, in turn, suggests elevated atmospheric Hg during the T-OAE.
480 Considering that 183 Ma marks the active periods of the Ferrar LIPs, while the Eastern Tethys
481 region experienced no significant LIP activity (Bergman et al., 2021; Heimdal et al., 2021), the Hg
482 enrichments in the Sichuan Basin can be tied to the large-scale activity of the Ferrar LIP. Therefore,
483 even though the X3 core shows evidence of an enhanced terrestrial input, the terrestrial Hg source
484 likely originated from plant and soil uptake of Hg released into the atmosphere by Ferrar LIP

activity., although this remains a plausible interpretation rather than a definitive conclusion. Thus, both atmospheric Hg deposition and terrestrial input likely played important roles in the global enrichment of Hg during the T-OAE (Figs. 2 and 4). Moreover, the pulsed Hg enrichment observed in both drill cores from the Sichuan Basin during the T-OAE, especially in the deep LQ104X core, which was minimally influenced by terrestrial Hg input, suggests potential episodic activity of the Ferrar LIP.

Additionally, the Ordos Basin, the east tributary of Bighorn Creek, Canada, and the shallow X3 core from the Sichuan Basin all show negative Hg isotope excursions during the T-OAE, but the magnitude of the negative excursion varies significantly across the three basins (Them et al., 2019; Jin et al., 2022). The Ordos Basin and X3 core in the Sichuan Basin both exhibit a negative excursion of 0.06‰, whereas the east tributary of Bighorn Creek, Canada, exhibits a Δ^{199}Hg excursion of up to -0.4‰ (Them et al., 2019; Jin et al., 2022). Such a significant shift in Δ^{199}Hg value from the east tributary of Bighorn Creek may be attributed to mechanism other than an increased terrestrial Hg input. One plausible explanation is photochemical reduction of Hg^{2+} to Hg^0 during photic zone euxinia (Zheng and Hintelmann, 2009; Zheng et al., 2018). This hypothesis is supported by the relationships between Δ^{199}Hg and δ^{202}Hg, as well as between Δ^{199}Hg and Δ^{201}Hg. Photochemical reduction during photic zone euxinia usually generates a $\Delta^{199}Hg/\delta^{202}Hg$ slope of -0.7 and a $\Delta^{199}Hg/\Delta^{201}Hg$ ratio of 1.00 (Zheng and Hintelmann, 2009; Blum et al., 2014; Zheng et al., 2018). In the east tributary of Bighorn Creek, T-OAE samples exhibit a $\Delta^{199}Hg/\delta^{202}Hg$ slope of -0.63 (Fig. S10), and an average $\Delta^{199}Hg/\Delta^{201}Hg$ ratio of 1.05, confirming Hg^{2+} photochemical reduction during the T-OAE.

4.5. Potential Hg loss during the T-OAE

Despite our demonstration that large-scale activity of the Ferrar LIPs led to global Hg enrichment during the T-OAE, changes in global and local redox conditions may have resulted in changes in the behavior of Hg (Frieling et al., 2023). In particular, under ferruginous or weakly sulfidic conditions, Hg loss from the sediments could occur, potentially leading to an underestimation of the actual extent of Hg enrichment (Frieling et al., 2023; Zheng et al., 2023). Mercury (di)methylation mediated by iron-reducing bacteria and archaea (Fleming et al., 2006; Gilmour et al., 2013), as well as subsequent Hg-reduction processes, has been calculated to drive up to 65% loss of total Hg from sediments deposited under ferruginous or weakly sulfidic bottom waters (Frieling et al., 2023). Most T-OAE samples from the Sichuan basin appear to have been deposited under anoxic-ferruginous or weakly sulfidic conditions based on Fe speciation analyses and Mo_{EF} values (Liu et al., 2022; Li et al., 2023), supporting potential sedimentary Hg loss via Hg (di)methylation and Hg-reduction in the two basins (Fig. 6).

In the two cores from the Sichuan Basin and the Anya section in the Ordos Basin, correlation between Hg_{ex} and redox proxies (i.e., Fe_{py}/Fe_{HR} or Mo_{EF}; Fig. 5) generally follow a consistent pattern, with the exception of samples showing Hg_{ex} spikes. Initially, there are generally positive correlations, which then collapse and possibly even turn negative after reaching peak values (Fig. 5). This suggests the existence of a redox threshold, whereby below this threshold, Hg is buried, while Hg loss from the sediments is promoted above this threshold. A similar phenomenon has been observed in the Cleveland Basin of the Western Tethys (Fig. 5G), where a distinct negative correlation between Hg_{ex} and Mo_{EF} is evident when Mo_{EF} exceeds 4. This pattern implies potential sedimentary Hg loss via Hg (di)methylation and Hg-reduction. However, due to the absence of corresponding iron speciation data, the relationship between Hg_{ex} and Fe_{py}/Fe_{HR} cannot be evaluated.

5. Conclusions

Large-scale activity of the Ferrar LIP is clearly documented in the Sichuan Basin. However, there are differences in the pathways of Hg from the atmosphere to its deposition. Shallow areas received more terrestrial Hg, while deep areas received more atmospheric Hg. Nevertheless, the Hg sources to the Sichuan Basin were likely linked to Ferrar LIP emissions. Additionally, widespread Hg loss from the sediments or water column likely occurred due to (di)methylation and subsequent reduction under ferruginous or weakly sulfidic bottom water during the T-OAE, and consequently, Hg enrichment levels have likely been underestimated. This study thus resolves the role of enhanced volcanism as a driver for the T-OAE, while also providing more general insight into controls on Hg cycling during major geological events, highlighting the importance of detailed redox analyses for a comprehensive understanding of potential links between volcanism and Hg cycling.

CRediT authorship contribution statement

Jinchao Liu: Writing – original draft, Investigation, Data curation, Conceptualization. **Jian Cao:** Writing – original draft, Conceptualization, Supervision. **Simon W. Poulton:** Writing – review & editing, Conceptualization. **Wang Zheng:** Data curation. **Jiubin Chen:** Data curation. **Tianchen He:** Writing – review & editing. **Guang Hu:** Writing – review & editing. **Di Xiao:** Writing – review & editing.

Data availability

The original data generated in this study are provided in the Supplementary Data Files.

Acknowledgements

We thank Editor Dr. Tristan Horner and two anoymous reviewers for their constructive comments and suggestions for improving the manuscript. This work was funded by the National Natural Science Foundation of China (Grant Nos. 42230808 and U24A20593).

References

Alcott, L.J., Krause, A.J., Hammarlund, E.U., Bjerrum, C.J., Scholz, F., Xiong, Y., Hobson, A.J., Neve, L., Mills, B.J.W., März, C., Schnetger, B., Bekker, A., Poulton, S.W., 2020. Development of Iron Speciation Reference Materials for Palaeoredox Analysis. Geostandards and Geoanalytical Research 44, 581-591.

Algeo, T.J., Li, C., 2020. Redox classification and calibration of redox thresholds in sedimentary systems. Geochimica et Cosmochimica Acta 287, 8-26.

Bagnato, E., Tamburello, G., Avard, G., Martinez-Cruz, M., Enrico, M., Fu, X., Sprovieri, M., Sonke, J.E., 2014. Mercury fluxes from volcanic and geothermal sources: an update. Geological Society, London, Special Publications 410, 263-285.

Bergman, S.C., Eldrett, J.S., Minisini, D., 2021. Phanerozoic Large Igneous Province, Petroleum System, and Source Rock Links, Large Igneous Provinces, pp. 191-228.

Bergquist, B.A., Blum, J.D., 2007. Mass-dependent and -independent fractionation of hg isotopes by photoreduction in aquatic systems. Science 318, 417–420.

Blum, J.D., Bergquist, B.A., 2007. Reporting of variations in the natural isotopic composition of mercury. Anal Bioanal Chem 388, 353-359.

Blum, J.D., Sherman, L.S., Johnson, M.W., 2014. Mercury Isotopes in Earth and Environmental Sciences. Annual Review of Earth and Planetary Sciences 42, 249-269.

Brazier, J.-M., Suan, G., Tacail, T., Simon, L., Martin, J.E., Mattioli, E., Balter, V., 2015. Calcium isotope evidence for dramatic increase of continental weathering during the Toarcian oceanic anoxic event (Early Jurassic). Earth and Planetary Science Letters 411, 164-176.

Burgess, S.D., Bowring, S.A., Fleming, T.H., Elliot, D.H., 2015. High-precision geochronology links the Ferrar large igneous province with early-Jurassic ocean anoxia and biotic crisis. Earth and Planetary Science Letters 415, 90-99.

Canfield, D.E., Raiswell, R., Westrich, J.T., Reaves, C.M., Bener, R.A., 1986. The use of chromium reduction in the analysis of reduced sulfur in sediments and shales. Chemical Geology 54, 149–155.

Charbonnier, G., Föllmi, K.B., 2017. Mercury enrichments in lower Aptian sediments support the link between Ontong Java large igneous province activity and oceanic anoxic episode 1a. Geology 45, 63-66.

Chen, J., Hintelmann, H., Dimock, B., 2010. Chromatographic pre-concentration of Hg from dilute aqueous solutions for isotopic measurement by MC-ICP-MS. J. Anal. At. Spectrom. 25, 1402.

Chen, J., Hintelmann, H., Feng, X., Dimock, B., 2012. Unusual fractionation of both odd and even mercury isotopes in precipitation from Peterborough, ON, Canada. Geochimica et Cosmochimica Acta 90, 33-46.

Chen, J., Sun, G., Lu, B., Ma, R.-y., Xiao, Z., Cai, Y.-f., Zhang, H., Shen, S.-z., Zhang, F., Feng, Z., 2023. Inconsistent mercury records from terrestrial upland to coastal lowland across the Permian-Triassic transition. Earth and Planetary Science Letters 614, 118195.

Clarkson, M.O., Poulton, S.W., Guilbaud, R., Wood, R.A., 2014. Assessing the utility of Fe/Al and Fe-speciation to record water column redox conditions in carbonate-rich sediments. Chemical Geology 382, 111-122.

Corso, J., Mills, B.J.W., Chu, D., Newton, R.J., Mather, T.A., Shu, W., Wu, Y., Tong, J., Wignall, P.B., 2020. Permo-Triassic boundary carbon and mercury cycling linked to terrestrial ecosystem collapse. Nat Commun 11, 2962.

Dera, G., Pucéat, E., Pellenard, P., Neige, P., Delsate, D., Joachimski, M.M., Reisberg, L., Martinez, M., 2009. Water mass exchange and variations in seawater temperature in the NW Tethys during the Early Jurassic: Evidence from neodymium and oxygen isotopes of fish teeth and belemnites. Earth and Planetary Science Letters 286, 198-207.

Edwards, B.A., Kushner, D.S., Outridge, P.M., Wang, F., 2021. Fifty years of volcanic mercury emission research: Knowledge gaps and future directions. Science of The Total Environment 757.

Fendley, I.M., Frieling, J., Mather, T.A., Ruhl, M., Hesselbo, S.P., Jenkyns, H.C., 2024. Early Jurassic large igneous province carbon emissions constrained by sedimentary mercury. Nature Geoscience 17, 241-248.

Feng, R., Wu, Y., Tao, S., Zhang, T., Yue, T., Yang, J., Liu, M., 2015. Sedimentary microfacies characteristics and their control on reservoirs in Da'anzhai Member, lower Jurassic, Sichuan Basin. Petroleum Geology and Experiment 37, 320-328.

Fernández-Martínez, J., Ruíz, F.M., Rodríguez-Tovar, F.J., Piñuela, L., García-Ramos, J.C., Algeo, T.J., 2023. Euxinia and hydrographic restriction in the Tethys Ocean: Reassessing global oceanic anoxia during the early Toarcian. Global and Planetary Change 221, 104026.

Fernandez, A., Korte, C., Ullmann, C.V., Looser, N., Wohlwend, S., Bernasconi, S.M., 2021. Reconstructing the magnitude of Early Toarcian (Jurassic) warming using the reordered clumped isotope compositions of belemnites. Geochimica et Cosmochimica Acta 293, 308-327.

Fleming, E.J., Mack, E.E., Green, P.G., Nelson, D.C., 2006. Mercury methylation from unexpected sources: molybdate-inhibited freshwater sediments and an iron-reducing bacterium. Appl Environ Microbiol 72, 457-464.

Font, E., Chen, J., Regelous, M., Regelous, A., Adatte, T., 2021. Volcanic origin of the mercury anomalies at the Cretaceous-Paleogene transition of Bidart, France. Geology 50, 142-146.

Font, E., Duarte, L.V., Dekkers, M.J., Remazeilles, C., Egli, R., Spangenberg, J.E., Fantasia, A., Ribeiro, J., Gomes, E., Mirao, J., Adatte, T., 2022. Rapid light carbon releases and increased aridity linked to Karoo-Ferrar magmatism during the early Toarcian oceanic anoxic event. Sci Rep 12, 4342.

Frieling, J., Mather, T.A., März, C., Jenkyns, H.C., Hennekam, R., Reichart, G.J., Slomp, C.P., van Helmond, N.A.G.M., 2023. Effects of redox variability and early diagenesis on marine sedimentary Hg records. Geochimica et Cosmochimica Acta 351, 78-95.

Frimmel, H.E., 2009. Trace element distribution in Neoproterozoic carbonates as palaeoenvironmental indicator. Chem. Geol. 258, 338-353.

Gilmour, C.C., Podar, M., Bullock, A.L., Graham, A.M., Brown, S.D., Somenahally, A.C., Johs, A., Hurt, R.A., Jr., Bailey, K.L., Elias, D.A., 2013. Mercury methylation by novel microorganisms from new environments. Environ Sci Technol 47, 11810-11820.

Grasby, S.E., Sanei, H., Beauchamp, B., Chen, Z., 2013. Mercury deposition through the Permo–Triassic Biotic Crisis. Chemical Geology 351, 209-216.

Grasby, S.E., Shen, W., Yin, R., Gleason, J.D., Blum, J.D., Lepak, R.F., Hurley, J.P., Beauchamp, B., 2017. Isotopic signatures of mercury contamination in latest Permian oceans. Geology 45, 55-58.

Grasby, S.E., Them, T.R., Chen, Z., Yin, R., Ardakani, O.H., 2019. Mercury as a proxy for volcanic emissions in the geologic record. Earth-Science Reviews 196, 102880.

He, T., Wignall, P.B., Newton, R.J., Atkinson, J.W., Keeling, J.F.J., Xiong, Y., Poulton, S.W., 2022. Extensive marine anoxia in the European epicontinental sea during the end-Triassic mass extinction. Global and Planetary Change 210.

Heimdal, T.H., Godderis, Y., Jones, M.T., Svensen, H.H., 2021. Assessing the importance of thermogenic degassing from the Karoo Large Igneous Province (LIP) in driving Toarcian carbon cycle perturbations. Nat Commun 12, 6221.

Hermoso, M., Minoletti, F., Le Callonnec, L., Jenkyns, H.C., Hesselbo, S.P., Rickaby, R.E.M., Renard, M., de Rafélis, M., Emmanuel, L., 2009. Global and local forcing of Early Toarcian seawater chemistry: A comparative study of different paleoceanographic settings (Paris and Lusitanian basins). Paleoceanography 24, PA4208.

Hesselbo, S.P., Gröcke, D.R., Jenkyns, H.C., Bjerrum, C.J., Farrimond, P., Bell, H.S.M., Green, O.R., 2000. Massive dissociation of gas hydrate during a Jurassic oceanic anoxic event. Nature 406, 392-395.

Jenkyns, H.C., 2010. Geochemistry of oceanic anoxic events. Geochemistry, Geophysics, Geosystems 11, Q03004.

Jin, X., Zhang, F., Baranyi, V., Kemp, D.B., Feng, X., Grasby, S.E., Sun, G., Shi, Z., Chen, W., Dal Corso, J., 2022. Early Jurassic massive release of terrestrial mercury linked to floral crisis. Earth and Planetary Science Letters 598, 117842.

Kamber, B.S., Bolhar, R., 2004. Geochemistry of late Archaean stromatolites from Zimbabwe: evidence for microbial life in restricted epicontinental seas. Precambrian Res. 132, 379-399.

Kamber, B.S., Webb, G.E., 2001. The geochemistry of late Archaean microbial carbonate: implications for ocean chemistry and continental erosion history. Geochim. Cosmochim. Acta 65, 2509–2525.

Kemp, D.B., Ramezani, J., Izumi, K., Al-Suwaidi, A., Huang, C., Chen, W., Zhu, Y., 2024. The timing and duration of large-scale carbon release in the Early Jurassic. Geology 52, 891-895.

Li, B., Jin, X., Corso, J.D., Ogg, J.G., Lang, X., Baranyi, V., Preto, N., Franceschi, M., Qiao, P., Shi, Z., 2023. Complex pattern of environmental changes and organic matter preservation in the NE Ordos lacustrine depositional system (China) during the T-OAE (Early Jurassic) Global and Planetary Change 221, 104045.

Li, S., Wignall, P.B., Xiong, Y., Poulton, S.W., 2024. Calibration of redox thresholds in black shale: Insight from a stratified Mississippian basin with warm saline bottom waters. Bulletin 136, 1266-1286.

Li, X., 2016. The study of cyclostratigraphy in the Da'anzhai Member of the Gong 39 core area in the central Sichuan Basin. master's degree.

Li, Y., He, D., 2014. Evolution of tectonic-depositional environment and prototype basins of the Early Jurassic in Sichuan Basin and adjacent areas. Acta Pet. Sin. 35, 219-232.

Liu, J., Cao, J., He, T., Liang, F., Pu, J., Wang, Y., 2022. Lacustrine redox variations in the Toarcian Sichuan Basin across the Jenkyns Event. Global and Planetary Change 215, 103860.

Liu, J., Cao, J., Hu, G., Wang, Y., Yang, R., Liao, Z., 2020. Water-level and redox fluctuations in a Sichuan Basin lacustrine system coincident with the Toarcian OAE. Palaeogeography, Palaeoclimatology, Palaeoecology 558, 109942.

McElwain, J.C., Wade-Murphy, J., Hesselbo, S.P., 2005. Changes in carbon dioxide during an oceanic anoxic event linked to intrusion into Gondwana coals. Nature 435, 479-482.

Moulin, M., Fluteau, F., Courtillot, V., Marsh, J., Delpech, G., Quidelleur, X., Gérard, M., Jay, A.E., 2011. An attempt to constrain the age, duration, and eruptive history of the Karoo flood basalt: Naude's Nek section (South Africa). Journal of Geophysical Research 116, 738-772.

Outridge, P.M., Sanei, H., Stern, G.A., Hamilton, P.B., Goodarzi, F., 2007. Evidence for control of mercury accumulation rates in Canadian High Arctic Lake sediments by variations of aquatic primary productivity. Environmental Science and Technology 41, 5259–5265.

Percival, L.M.E., Jenkyns, H.C., Mather, T.A., Dickson, A.J., Batenburg, S.J., Ruhl, M., Hesselbo, S.P., Barclay, R., Jarvis, I., Robinson, S.A., Woelders, L., 2018. Does large igneous province volcanism always perturb the mercury cycle? Comparing the records of Oceanic Anoxic Event 2 and the end-Cretaceous to other Mesozoic events. American Journal of Science 318, 799-860.

Percival, L.M.E., Witt, M.L.I., Mather, T.A., Hermoso, M., Jenkyns, H.C., Hesselbo, S.P., Al-Suwaidi, A.H., Storm, M.S., Xu, W., Ruhl, M., 2015. Globally enhanced mercury deposition during the end-Pliensbachian extinction and Toarcian OAE: A link to the Karoo–Ferrar Large Igneous Province. Earth and Planetary Science Letters 428, 267-280.

Poulton, S., Raiswell, R., 2002. The low-temperature geochemical cycle of iron: from continental fluxes to marine sediment deposition. American journal of science 302, 774-805.

Poulton, S.W., 2021. The Iron Speciation Paleoredox Proxy. Cambridge University Press.

Poulton, S.W., Canfield, D.E., 2005. Development of a sequential extraction procedure for iron: implications for iron partitioning in continentally derived particulates. Chemical Geology 214, 209-221.

Poulton, S.W., Canfield, D.E., 2011. Ferruginous Conditions: A Dominant Feature of the Ocean through Earth's History. Elements 7, 107-112.

Pyle, D.M., Mather, T.A., 2003. The importance of volcanic emissions for the global atmospheric mercury cycle. Atmospheric Environment 37, 5115-5124.

Qin, X., Cao, J., Luo, B., Liu, J., Hu, G., 2025. Sulfate concentration and redox state control the pyrite formation and sulfur cycle in a T-OAE lake, Sichuan Basin, China. Chemical Geology 676.
Raiswell, R., Canfield, D.E., 1998. Sources of iron for pyrite formation in marine sediments. American Journal of Science 298, 219-245.
Ravichandran, M., 2004. Interactions between mercury and dissolved organic matter--a review. Chemosphere 55, 319-331.
Riding, J.B., Walton, W., Shaw, D., 1991. Toarcian to Bathonian (Jurassic) palynology of the Inner Hebrides, northwest Scotland. Palynology 15, 115-79.
Rudnick, R.L., Gao, S., 2014. Composition of the Continental Crust, Treatise on Geochemistry, pp. 1-51.
Ruebsam, W., Pieńkowski, G., Schwark, L., 2020. Toarcian climate and carbon cycle perturbations – its impact on sea-level changes, enhanced mobilization and oxidation of fossil organic matter. Earth and Planetary Science Letters 546, 116417.
Sanei, H., Grasby, S.E., Beauchamp, B., 2011. Latest Permian mercury anomalies. Geology 40, 63-66.
Shen, J., Chen, J., Algeo, T.J., Feng, Q., Yu, J., Xu, Y.-G., Xu, G., Lei, Y., Planavsky, N.J., Xie, S., 2020a. Mercury fluxes record regional volcanism in the South China craton prior to the end-Permian mass extinction. Geology 49, 452-456.
Shen, J., Chen, J., Algeo, T.J., Yuan, S., Feng, Q., Yu, J., Zhou, L., O'Connell, B., Planavsky, N.J., 2019. Evidence for a prolonged Permian-Triassic extinction interval from global marine mercury records. Nat Commun 10, 1563.
Shen, J., Feng, Q., Algeo, T.J., Liu, J., Zhou, C., Wei, W., Liu, J., Them, T.R., Gill, B.C., Chen, J., 2020b. Sedimentary host phases of mercury (Hg) and implications for use of Hg as a volcanic proxy. Earth and Planetary Science Letters 543.
Shen, J., Yin, R., Algeo, T.J., Svensen, H.H., Schoepfer, S.D., 2022. Mercury evidence for combustion of organic-rich sediments during the end-Triassic crisis. Nat Commun 13, 1307.
Shi, M., Bergquist, B.A., Zhou, A., Zhao, Y., Sun, R., J., C., W., Z., 2023. The efficiency of Hg cold vapor generation and its influence on Hg isotope analysis by MC-ICP-MS. J. Anal. At. Spectrom. 38, 1076–1087.
Srivastava, S.K., 1987. Jurassic spore-pollen assemblages from Normandy (France) and Germany. Geobios 20, 5-79.
Srivastava, S.K., 2011. Spore-pollen biostratigraphy of the English Jurassic. Palaeontographica Abteilung B 285, 113-201.
Taylor, S.R., McLennan, S.M., 1985. The Continental Crust: Its Composition and Evolution. Blackwell, Oxford, p. 312.
Them, T.R., Jagoe, C.H., Caruthers, A.H., Gill, B.C., Grasby, S.E., Gröcke, D.R., Yin, R., Owens, J.D., 2019. Terrestrial sources as the primary delivery mechanism of mercury to the oceans across the Toarcian Oceanic Anoxic Event (Early Jurassic). Earth and Planetary Science Letters 507, 62-72.
Tribovillard, N., Algeo, T.J., Lyons, T., Riboulleau, A., 2006. Trace metals as paleoredox and paleoproductivity proxies: An update. Chemical Geology 232, 12-32.
Tribovillard, N., du Châtelet, E.A., Gay, A., Barbecot, F., Sansjofre, P., Potdevin, J.-L., 2013. Geochemistry of cold seepage-impacted sediments: Per-ascensum or per-descensum trace metal enrichment? Chemical Geology 340, 1-12.
Wang, Y., Wignall, P.B., Xiong, Y., Loydell, D.K., Peakall, J., Baas, J.H., Mills, B.J.W., Poulton, S.W., 2024. Marine redox dynamics and biotic response to the mid-Silurian Ireviken Extinction Event in a mid-shelf setting. Journal of the Geological Society 181.
Xu, W., Ruhl, M., Jenkyns, Hugh C., Hesselbo, Stephen P., Riding, James B., Selby, D., Naafs, B.David A., Weijers, Johan W.H., Pancost, Richard D., Tegelaar, Erik W., Idiz, Erdem F., 2017. Carbon sequestration in an expanded lake system during the Toarcian oceanic anoxic event. Nature Geoscience 10, 129-134.
Xu, W., Ruhl, M., Jenkyns, H.C., Leng, M.J., Huggett, J.M., Minisini, D., Ullmann, C.V., Riding, J.B., Weijers, J.W.H., Storm, M.S., Percival, L.M.E., Tosca, N.J., Idiz, E.F., Tegelaar, E.W., Hesselbo, S.P., 2018. Evolution of the

740 Toarcian (Early Jurassic) carbon-cycle and global climatic controls on local sedimentary processes (Cardigan Bay
741 Basin, UK). Earth and Planetary Science Letters 484, 396-411.
742 Yin, R., Feng, X., Hurley, J.P., Krabbenhoft, D.P., Lepak, R.F., Hu, R., Zhang, Q., Li, Z., Bi, X., 2016. Mercury Isotopes
743 as Proxies to Identify Sources and Environmental Impacts of Mercury in Sphalerites. Sci Rep 6, 18686.
744 Zerkle, A.L., Yin, R., Chen, C., Li, X., Izon, G.J., Grasby, S.E., 2020. Anomalous fractionation of mercury isotopes in
745 the Late Archean atmosphere. Nat Commun 11, 1709.
746 Zheng, R., 1998. High-Resolution Sequence Stratigraphy of Da'anzhai Formation, Lower Jurassic in Sichuan Basin.
747 Acta Sedimentologica Sinica 16, 42-49.
748 Zheng, W., Gilleaudeau, G.J., Algeo, T.J., Zhao, Y., Song, Y., Zhang, Y., Sahoo, S.K., Anbar, A.D., Carmichael, S.K.,
749 Xie, S., Liu, C.-Q., Chen, J., 2023. Mercury isotope evidence for recurrent photic-zone euxinia triggered by
750 enhanced terrestrial nutrient inputs during the Late Devonian mass extinction. Earth and Planetary Science Letters
751 613, 118175.
752 Zheng, W., Gilleaudeau, G.J., Kah, L.C., Anbar, A.D., 2018. Mercury isotope signatures record photic zone euxinia in
753 the Mesoproterozoic ocean. Proc Natl Acad Sci U S A 115, 10594-10599.
754 Zheng, W., Hintelmann, H., 2009. Mercury isotope fractionation during photoreduction in natural water is controlled by
755 its Hg/DOC ratio. Geochimica et Cosmochimica Acta 73, 6704-6715.
756 Zhou, Y., Li, Y., Zheng, W., Tang, S., Pan, S., Chen, J., He, X.-F., Shen, J., Algeo, T.J., 2024. The role of LIPs in
757 Phanerozoic mass extinctions: An Hg perspective. Earth-Science Reviews 249, 104667.
758

Figure captions:

Fig. 1. Maps of the Sichuan Basin during the Early Jurassic. Geo-map adapted from Ron Blakey https://deeptimemaps.com/, (©2016 Colorado Plateau Geosystems Inc.) (A) Location of the Sichuan Basin during the Early Jurassic (Xu et al., 2017). (B) Sedimentary environments of the Sichuan Basin, and the paleogeographic locations of the X3 and LQ104X cores. (C) Bathymetric positions of the X3 and LQ104X cores in the Sichuan Basin. 1=East Tributary Bighorn Creek, Alberta, Canada; 2= Anya section, Ordos Basin, China; 3= Mochras, Cardigan Bay Basin, United Kingdom; 4= Bornholm, Danish Basin, Denmark; 5= Peniche, Lusitanian Basin, Portugal; 6= El peñon, Chile; 7= Arroyo Lapa, Neuquén Basin, Argentina; 8= Hawsker Bottoms, Cleveland Basin, United Kingdom; 9=Dotternhausen quarry, southwest Germany; 10= Sancerre, Paris Basin, France; 11= Velebit, Adriatic Basin, Croatia. Orange circled numbers show locations where Hg enrichment has been identified.

Fig. 2. Variability in redox conditions (documented by Fe_{HR}/Fe_T, Fe_{py}/Fe_{HR}, U_{EF} and Mo_{EF}) and mercury cycling (documented by [Hg], Hg/TOC, Hg_{ex}, $\delta^{202}Hg$, $\Delta^{199}Hg$ and $\Delta^{200}Hg$) in the Toarcian Da'anzhai Member in the Sichuan Basin. The yellow shaded field represents the duration of the T-OAE. Dashed lines on Fe_{HR}/Fe_T plots represent calibrated boundaries for oxic (<0.22) and anoxic (>0.38) deposition, and on Fe_{py}/Fe_{HR} plots represent ferruginous (<0.6) and euxinic (>0.8) deposition (for anoxic samples only), with intermediate values considered equivocal(Poulton and Canfield, 2011; Poulton, 2021). Dashed lines on U_{EF} and Mo_{EF} plots represent regional oxic baseline values (see Methods). Note that Hg_{ex} concentrations are not reported for samples with low TOC (< 0.3 wt.%) because Hg is difficult to bury under low TOC conditions (Sanei et al., 2011),

leading to inaccurate descriptions of Hg enrichment levels. A = atmospheric Hg deposition, T= terrestrial Hg input. The rightmost column summarizes the redox conditions of the water-column.

Fig. 3. Correlations between elemental Hg and its potential host phases, including organic matter, sulphide, and clay minerals. Data for panels A, B and C are from the shallow X3 core, and panels D, E and F are from the deep LQ104X core. The black, blue and red text represent correlations for all samples, non-T-OAE samples and T-OAE samples, respectively.

Fig. 4. Total organic carbon and Hg concentrations from (A) Yorkshire, U.K., (B) Sancerre, France and (C) Dotternhausen Germany. Dark yellow rectangles represent the T-OAE interval based on carbon isotope excursions(Percival et al., 2015; Them et al., 2019).

Fig. 5. Correlations between Hg_{ex} and both Mo_{EF} and Fe_{Py}/Fe_{HR} in the T-OAE intervals of the shallow X3 core (A and B) and deep LQ104X core (C and D) in the Sichuan Basin, Ordos Basin (E and F) and Yorkshire, UK (G). The dashed line represents the predicted threshold that contributes to Hg burial. To the left of the dashed line represents Hg burial, while to the right represents Hg loss from the sediments.

Fig. 6. Schematic illustration of Hg cycling in the Sichuan Basin during the T-OAE. The dashed arrows represent possible processes. MeHg = methylmercury; DMHg = dimethylmercury.

803

Fig. 1.

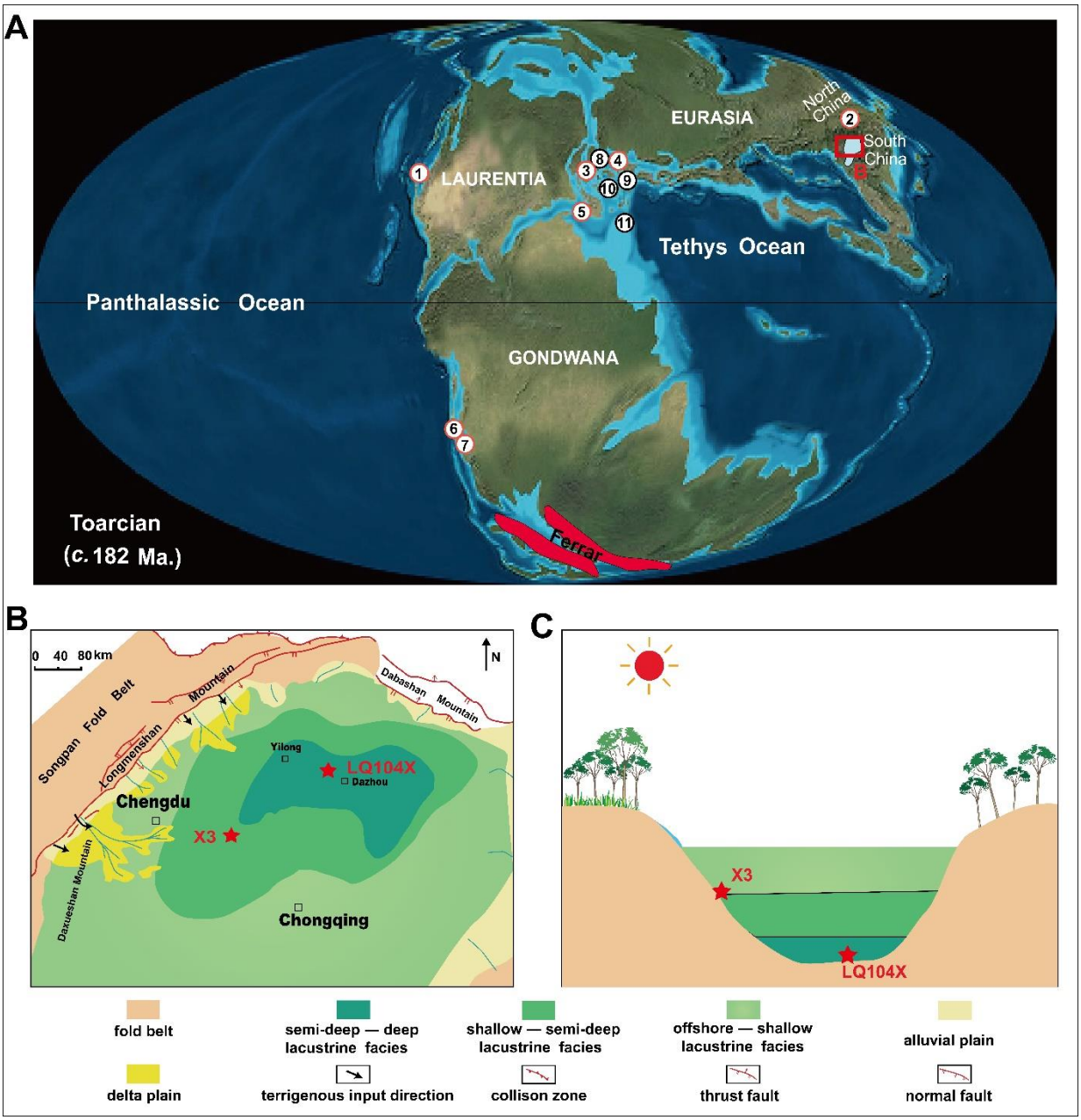

804
805

806

Fig. 2

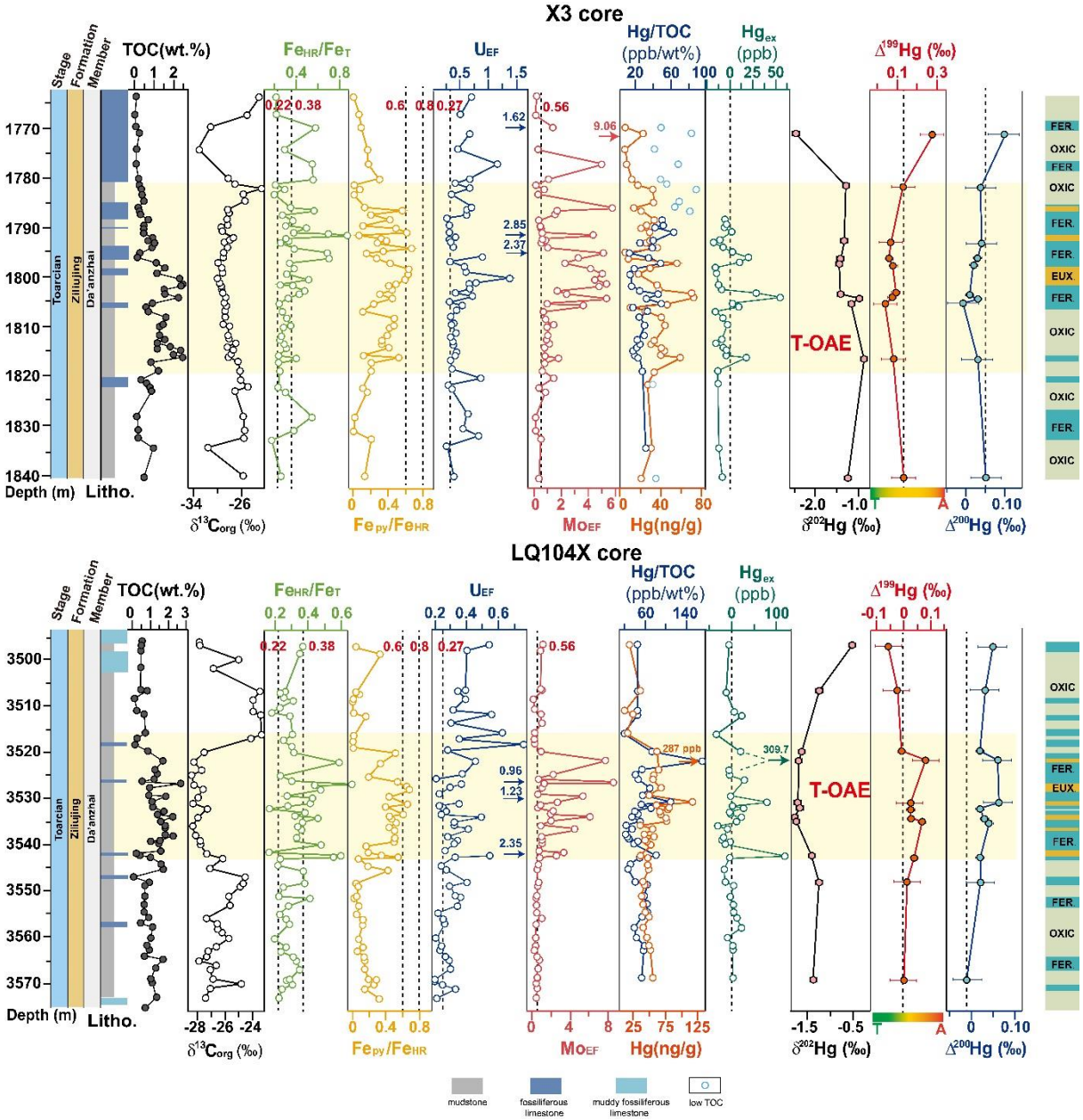

807

808

Fig. 3

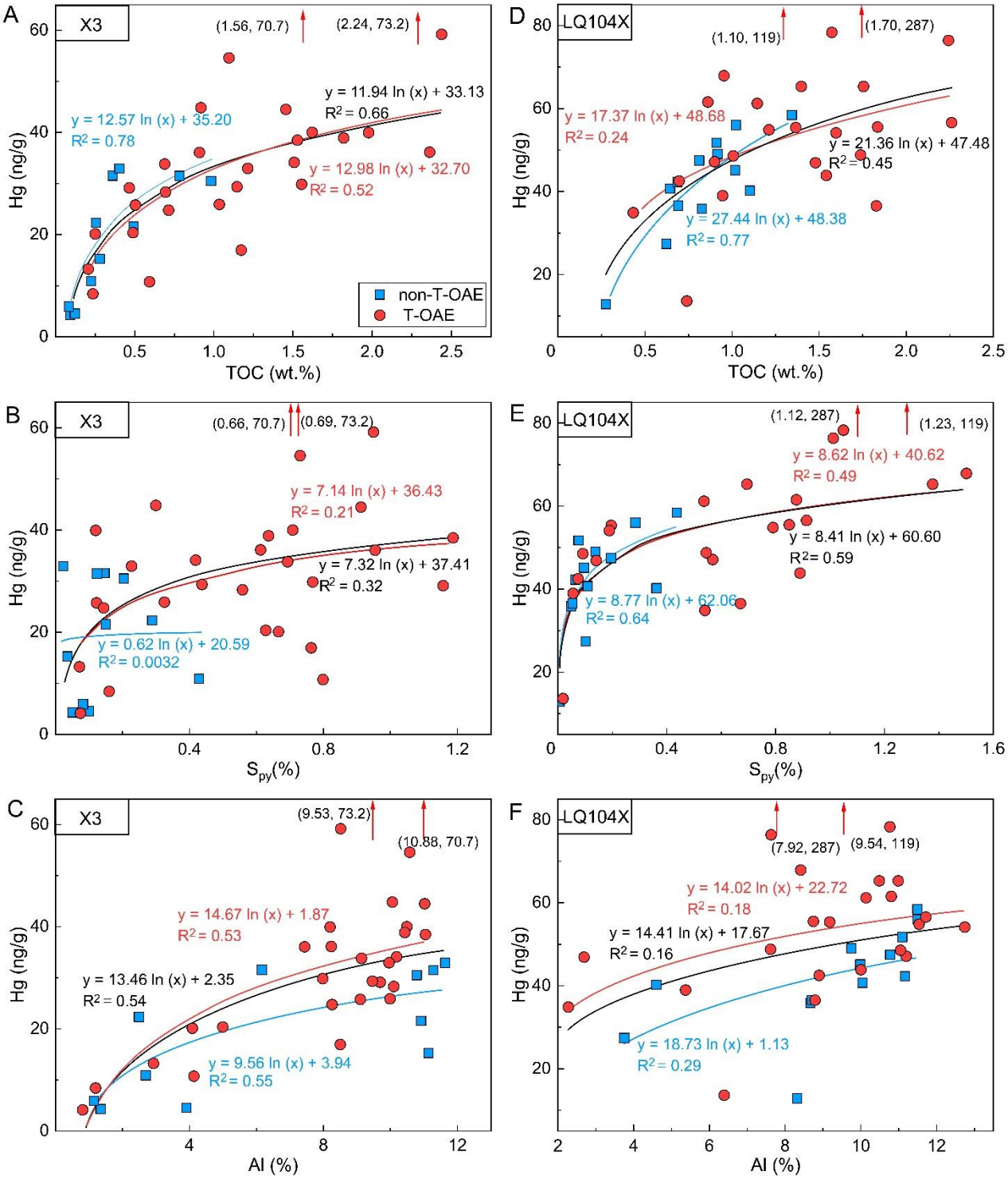
A
X3
(1.56, 70.7)
(2.24, 73.2)
y = 11.94 ln (x) + 33.13
R² = 0.66
y = 12.57 ln (x) + 35.20
R² = 0.78
y = 12.98 ln (x) + 32.70
R² = 0.52
non-T-OAE
T-OAE
Hg (ng/g)
TOC (wt.%)
D
LQ104X
(1.10, 119)
(1.70, 287)
y = 17.37 ln (x) + 48.68
R² = 0.24
y = 21.36 ln (x) + 47.48
R² = 0.45
y = 27.44 ln (x) + 48.38
R² = 0.77
Hg (ng/g)
TOC (wt.%)
B
X3
(0.66, 70.7)
(0.69, 73.2)
y = 7.14 ln (x) + 36.43
R² = 0.21
y = 7.32 ln (x) + 37.41
R² = 0.32
y = 0.62 ln (x) + 20.59
R² = 0.0032
Hg (ng/g)
S_py(%)
E
LQ104X
(1.12, 287)
(1.23, 119)
y = 8.62 ln (x) + 40.62
R² = 0.49
y = 8.41 ln (x) + 60.60
R² = 0.59
y = 8.77 ln (x) + 62.06
R² = 0.64
Hg (ng/g)
S_py(%)
C
X3
(9.53, 73.2)
(10.88, 70.7)
y = 14.67 ln (x) + 1.87
R² = 0.53
y = 13.46 ln (x) + 2.35
R² = 0.54
y = 9.56 ln (x) + 3.94
R² = 0.55
Hg (ng/g)
Al (%)
F
LQ104X
(7.92, 287)
(9.54, 119)
y = 14.02 ln (x) + 22.72
R² = 0.18
y = 14.41 ln (x) + 17.67
R² = 0.16
y = 18.73 ln (x) + 1.13
R² = 0.29
Hg (ng/g)
Al (%)

812

Fig. 4

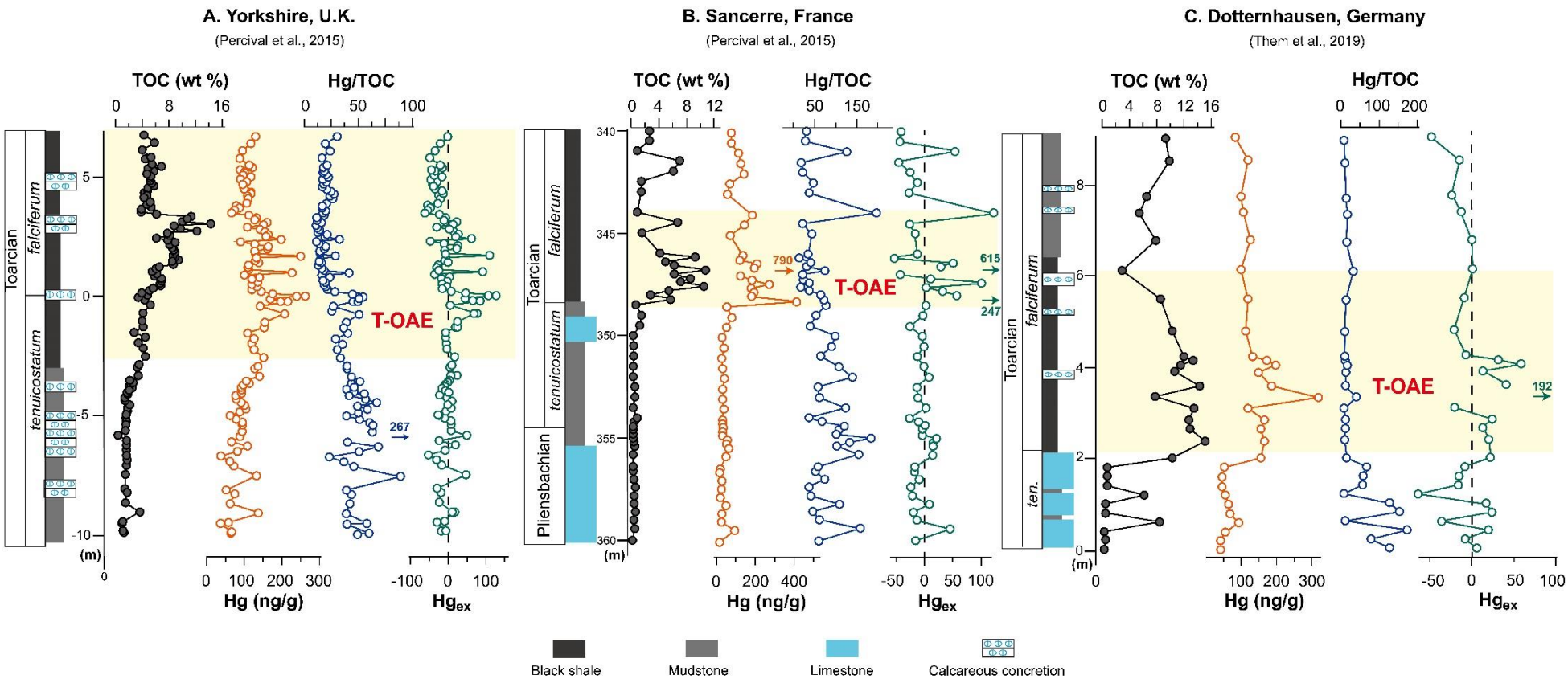

813

814

Fig. 5

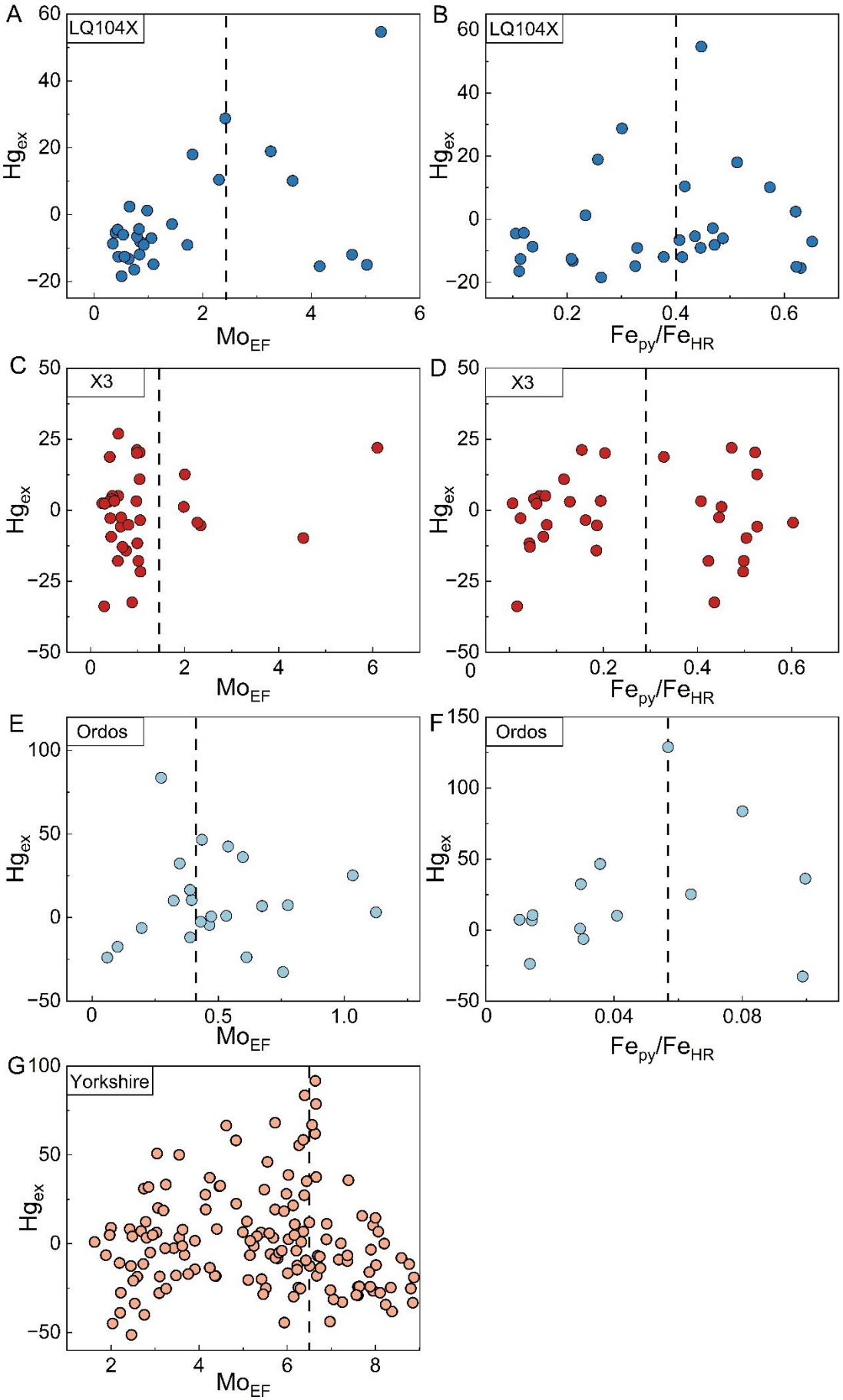
A
LQ104X
Hg_ex
Mo_EF
B
LQ104X
Hg_ex
Fe_py/Fe_HR
C
X3
Hg_ex
Mo_EF
D
X3
Hg_ex
Fe_py/Fe_HR
E
Ordos
Hg_ex
Mo_EF
F
Ordos
Hg_ex
Fe_py/Fe_HR
G
Yorkshire
Hg_ex
Mo_EF

Fig. 6

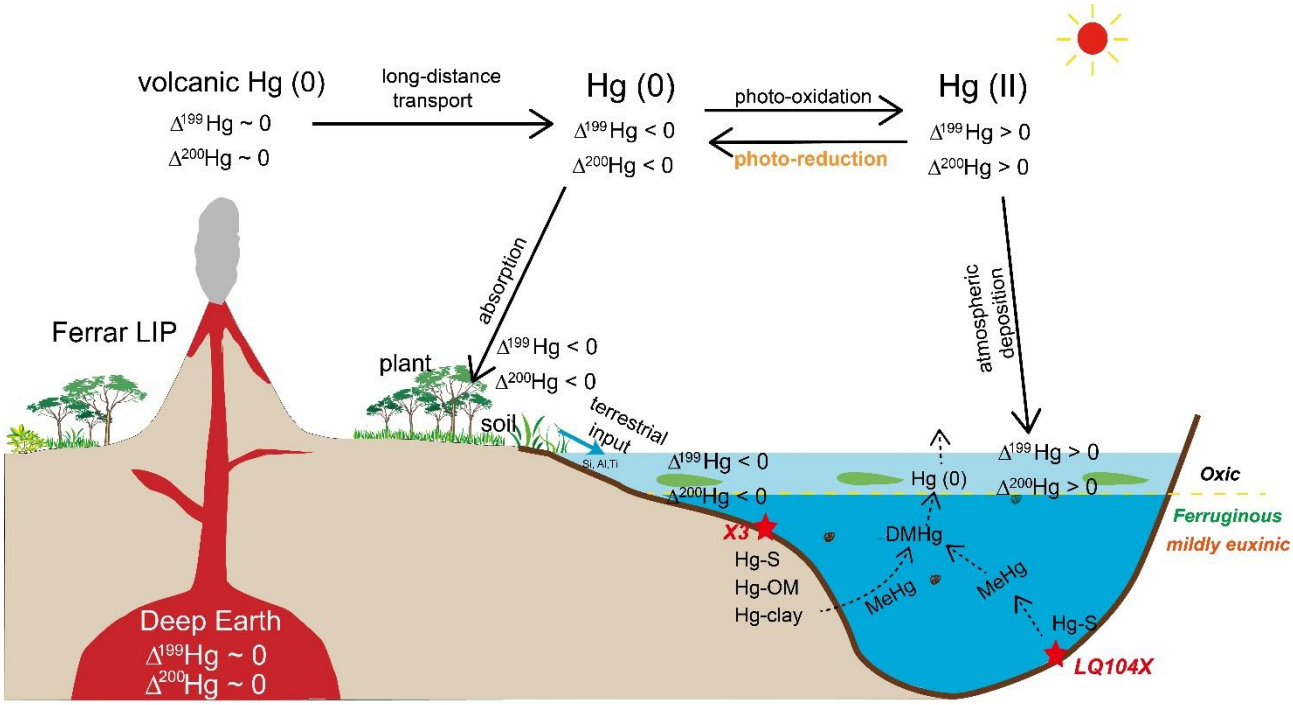
volcanic Hg (0)
Δ199Hg ~ 0
Δ200Hg ~ 0
long-distance transport
Hg (0)
Δ199Hg < 0
Δ200Hg < 0
photo-oxidation
photo-reduction
Hg (II)
Δ199Hg > 0
Δ200Hg > 0
absorption
atmospheric deposition
Ferrar LIP
plant
soil
terrestrial input
Si, Al,Ti
Δ199Hg < 0
Δ200Hg < 0
Hg (0)
Δ199Hg > 0
Δ200Hg > 0
Oxic
Ferruginous
mildly euxinic
X3
Hg-S
Hg-OM
Hg-clay
DMHg
MeHg
MeHg
Hg-S
LQ104X
Deep Earth
Δ199Hg ~ 0
Δ200Hg ~ 0